Spreading with evaporation and condensation in one-component fluids

Ryohei Teshigawara and Akira Onuki
Department of Physics, Kyoto University, Kyoto 606-8502, Japan

(Received 3 May 2010; revised manuscript received 23 June 2010; published 11 August 2010)

We investigate the dynamics of spreading of a small liquid droplet in gas in a one-component simple fluid, where the temperature is inhomogeneous around $0.9T_c$ and latent heat is released or generated at the interface upon evaporation or condensation (with T_c being the critical temperature). In the scheme of the dynamic van der Waals theory, the hydrodynamic equations containing the gradient stress are solved in the axisymmetric geometry. We assume that the substrate has a finite thickness and its temperature obeys the thermal diffusion equation. A precursor film then spreads ahead of the bulk droplet itself in the complete wetting condition. Cooling the substrate enhances condensation of gas onto the advancing film, which mostly takes place near the film edge and can be the dominant mechanism of the film growth in a late stage. The generated latent heat produces a temperature peak or a hot spot in the gas region near the film edge. On the other hand, heating the substrate induces evaporation all over the interface. For weak heating, a steady-state circular thin film can be formed on the substrate. For stronger heating, evaporation dominates over condensation, leading to eventual disappearance of the liquid region.

DOI: 10.1103/PhysRevE.82.021603 PACS number(s): 68.03.Fg, 68.08.Bc, 44.35.+c, 64.70.F−

I. INTRODUCTION

Extensive efforts have been made on the static and dynamic properties of wetting transitions for various fluids and substrates both theoretically and experimentally [1]. In particular, spreading of a liquid has been studied by many groups [1–8] since it is of great importance in a number of practical situations such as lubrication, adhesion, and painting. Hydrodynamic theories were developed for spreading of an involatile liquid droplet in gas in an early stage of the theoretical research [1,4,7–9]. A unique feature revealed by experiments [2,10–13] is that a thin precursor film is formed ahead of the liquid droplet itself in the complete wetting condition. Hardy first reported its formation ascribing its origin to condensation at the film edge [2], but it has been observed also for involatile fluids [10–13]. To understand nanometer-scale spreading processes, a number of microscopic simulations have been performed mainly for fluids composed of chainlike molecules [14–21].

However, understanding of the wetting dynamics of volatile liquids is still inadequate. We mention some examples where evaporation and condensation come into play. In their molecular-dynamics simulation [19], Koplik *et al.* observed evaporation of a droplet and a decrease in the contact angle upon heating a substrate in the partial wetting condition. In their experiment [22], Guéna *et al.* observed that a weakly volatile droplet spread as an involatile droplet in an initial stage but disappeared after a long time due to evaporation in the complete wetting condition. In a near-critical one-component fluid [23], Hegseth *et al.* observed that a bubble was attracted to a heated wall even when it was completely wetted by liquid in equilibrium (at zero heat flux), where the apparent contact angle of a bubble increased with the heat flux.

In addition to spreading on a heated or cooled substrate, there are a variety of situations such as droplet evaporation [24–28], boiling on a heated substrate [29–31], and motion of a bubble suspended in liquid [32,33], where latent heat generated or released at the interface drastically influences the hydrodynamic processes. In particular, a large temperature gradient and a large heat flux should be produced around the edge of a liquid film or the contact line of a droplet or bubble on a substrate [28,30]. The temperature and velocity profiles should be highly singular in these narrow regions. Here, an experiment by Höhmann and Stephan [31] is noteworthy. They observed a sharp drop in the substrate temperature near the contact line of a growing bubble in boiling. Furthermore, we should stress relevance of the Marangoni flow in multicomponent fluids in two-phase hydrodynamics [25,29,34], where temperature and concentration variations cause a surface tension gradient and a balance of the tangential stress induces a flow on the droplet scale.

In hydrodynamic theories, the gas-liquid transition has been included with the aid of a phenomenological input of the evaporation rate on the interface J. Some authors [24–26] assumed the form $J(r,t)=J_0/[r_e(t)^2-r^2]^{1/2}$ for a thin circular droplet as a function of the distance r from the droplet center, where $r_e(t)$ is the film radius and J_0 is a constant [35]. In the framework of the lubrication theory, Anderson and Davis [36] examined spreading of a thin volatile droplet on a heated substrate by assuming the form $J=(T_I-T_{\rm cx})/K^*$, where T_I is the interface temperature, $T_{\rm cx}$ is the saturation (coexistence) temperature, and K^* is a kinetic coefficient. In these papers, the dynamical processes in the gas have been neglected.

Various mesoscopic (coarse-grained) simulation methods have also been used to investigate two-fluid hydrodynamics, where the interface has a finite thickness. We mention phase field models of fluids (mostly treating incompressible binary mixtures) [37–52], where the gradient stress is included in the hydrodynamic equations (see a review in Ref. [39]). In particular, some authors numerically studied liquid-liquid phase separation in heat flow [38,43,47,51], but these authors treated symmetric binary mixtures without latent heat. Recently, one of the present authors developed a phase field model for compressible fluids with inhomogeneous temperature, which is called the dynamic van der Waals model

[48,49]. In its framework, we may describe gas-liquid transitions and convective latent heat transport without assuming any evaporation formula. In one of its applications [28], it was used to investigate evaporation of an axisymmetric droplet on a heated substrate in a one-component system. Our finding there is that evaporation occurs mostly near the contact line. We also mention the lattice Boltzmann method to simulate the continuum equations, where the molecular velocity takes discrete values [44–47,52]. However, this method has not yet been fully developed to describe evaporation and condensation.

In this paper, we will simulate spreading using the dynamic van der Waals model [48,49]. We will treat a one-component fluid in a temperature range around $0.9T_c$, where the gas and liquid densities are not much separated. Namely, we will approach the problem relatively close to the critical point. Then the mean free path in the gas is not long, so that the temperature may be treated to be continuous across an interface in nonequilibrium. When the gas is dilute, the phase field approach becomes more difficult to treat gas flow produced by evaporation and condensation. It is known that the temperature near an interface changes sharply in the gas over the mean free path during evaporation [53].

The organization of this paper is as follows. In Sec. II, we will present the dynamic equations with appropriate boundary conditions. In Sec. III, the simulation method will be explained. In Sec. IV, numerical results of spreading will be given for cooling and heating the substrate.

II. DYNAMIC VAN DER WAALS THEORY

When we discuss phase transitions with inhomogeneous temperature, the free-energy functional is not well defined. In such cases, we should start with an entropy functional including a gradient contribution, which is determined by the number density $n=n(\boldsymbol{r},t)$ and the internal energy density $e=e(\boldsymbol{r},t)$ in one-component fluids. Here, we present minimal forms of the entropy functional and the dynamic equations needed for our simulation.

A. Entropy formalism

We introduce a local entropy density $\hat{S}=\hat{S}(\boldsymbol{r},t)$ consisting of regular and gradient terms as [48,49]

$$\hat{S} = ns(n,e) - \tfrac{1}{2}C|\nabla n|^2. \tag{2.1}$$

Here $s=s(\boldsymbol{r},t)$ is the entropy per particle depending on n and e. The coefficient C of the gradient term can depend on n [49], but it will be assumed to be a positive constant independent of n. The gradient entropy is negative and is particularly important in the interface region. The entropy functional is the space integral $\mathcal{S}_b \equiv \int d\boldsymbol{r}\hat{S}$ in the bulk region. As a function of n and e, the temperature T is determined from

$$\frac{1}{T} = \left(\frac{\delta \mathcal{S}_b}{\delta e}\right)_n = n\left(\frac{\partial s}{\partial e}\right)_n. \tag{2.2}$$

The generalized chemical potential $\hat{\mu}$ including the gradient part is of the form

$$\hat{\mu} = -T\left(\frac{\delta \mathcal{S}_b}{\delta n}\right)_e = \mu - TC\nabla^2 n, \tag{2.3}$$

where $\mu=-T[\partial(ns)/\partial n]_e$ is the usual chemical potential per particle. In equilibrium T and $\hat{\mu}$ are homogeneous constants.

In the van der Waals theory [54], fluids are characterized by the molecular volume v_0 and the pair-interaction energy ϵ. As a function of n and e, s is written as

$$s = k_B \ln[(e/n + \epsilon v_0 n)^{3/2}(1/v_0 n - 1)] + s_0, \tag{2.4}$$

where $s_0/k_B=\ln[v_0(m/3\pi\hbar^2)^{3/2}]+5/2$ with m being the molecular mass. We define T as in Eq. (2.2) to obtain the well-known van der Waals expressions for the internal energy e and the pressure $p=n\mu+Tns-e$,

$$e = 3nk_BT/2 - \epsilon v_0 n^2, \tag{2.5}$$

$$p = nk_BT/(1 - v_0 n) - \epsilon v_0 n^2. \tag{2.6}$$

The critical density, temperature, and pressure read

$$n_c = 1/3v_0, \quad T_c = 8\epsilon/27k_B, \quad p_c = \epsilon/27v_0, \tag{2.7}$$

respectively. Macroscopic gas-liquid coexistence with a planar interface is realized for $T<T_c$ and at the saturated vapor pressure $p=p_{cx}(T)$.

With the introduction of the gradient entropy, there arises a length ℓ defined by

$$\ell = (C/2k_Bv_0)^{1/2}, \tag{2.8}$$

in addition to the molecular diameter $\sim v_0^{1/3}$. From Eq. (2.3) the correlation length ξ is defined by $\xi^{-2}=(\partial\mu/\partial n)_T/TC$, so ξ is proportional to ℓ as

$$\xi/\ell = n(2v_0k_BTK_T)^{1/2}, \tag{2.9}$$

where $K_T=(\partial n/\partial p)_T/n$ is the isothermal compressibility. The interface thickness is of order ξ in two-phase coexistence and the surface tension γ is estimated as

$$\gamma \sim k_BT(1 - T/T_c)^{3/2}\ell/v_0, \tag{2.10}$$

in the mean-field theory (see the Appendix). The ratio $\ell/v_0^{1/3}$ should be of order unity for real simple fluids. However, we may treat ℓ as an arbitrary parameter in our phase field scheme.

In our previous paper [49], the internal energy density contains a positive gradient part in addition to the regular part e expressed in terms of T and n as in Eq. (2.5). Namely, the total internal energy density is the sum $e+K|\nabla n|^2/2$, where the coefficient K may depend on n. The gradient term in the Helmholtz free-energy density is then of the form $M|\nabla n|^2/2$ with $M=CT+K$. In this paper, however, we assume $C>0$ and $K=0$ for simplicity, neglecting the gradient energy. This approximation should not affect the essential aspects of the dynamical effects in this paper.

B. Hydrodynamic equations

We set up the hydrodynamic equations from the principle of positive entropy production in nonequilibrium [55]. The mass density $\rho=mn$ obeys the continuity equation,

$$\frac{\partial}{\partial t}\rho = -\nabla\cdot(\rho\boldsymbol{v}), \tag{2.11}$$

where $\boldsymbol{v}$ is the velocity field assumed to vanish on all the boundaries. In the presence of an externally applied potential field $U(\boldsymbol{r})$ (per unit mass), we write the equation for the momentum density $\rho\boldsymbol{v}$ as

$$\frac{\partial}{\partial t}\rho\boldsymbol{v} = -\nabla\cdot(\rho\boldsymbol{v}\boldsymbol{v} + \overleftrightarrow{\Pi} - \overleftrightarrow{\sigma}) - \rho\nabla U. \tag{2.12}$$

In our previous work [49] we set $U=gz$ for a gravitational field with g being the gravity acceleration. We note that U may also represent the van der Waals interaction between the fluid particles and the solid depending the distance from the wall [1]. The stress tensor is divided into three parts. $\rho\boldsymbol{v}\boldsymbol{v}$ is the inertial part. $\overleftrightarrow{\Pi}=\{\Pi_{ij}\}$ is the reversible part including the gradient stress tensor,

$$\Pi_{ij} = \left[p - CT\left(n\nabla^2 n + \tfrac{1}{2}|\nabla n|^2\right)\right]\delta_{ij} + CT(\nabla_i n)(\nabla_j n), \tag{2.13}$$

where p is the van der Waals pressure in Eq. (2.6). Hereafter $\nabla_i=\partial/\partial x_i$ with x_i representing x, y, or z. $\overleftrightarrow{\sigma}=\{\sigma_{ij}\}$ is the viscous stress tensor expressed as

$$\sigma_{ij} = \eta(\nabla_i v_j + \nabla_j v_i) + (\zeta - 2\eta/3)(\nabla\cdot\boldsymbol{v})\delta_{ij}, \tag{2.14}$$

in terms of the shear viscosity η and the bulk viscosity ζ. Including the kinetic-energy density and the potential energy, we define the (total) energy density by $e_{\mathrm{T}}=e+\rho\boldsymbol{v}^2/2+\rho U$. It is a conserved quantity governed by [56]

$$\frac{\partial}{\partial t}e_{\mathrm{T}} = -\nabla\cdot[e_{\mathrm{T}}\boldsymbol{v} + (\overleftrightarrow{\Pi} - \overleftrightarrow{\sigma})\cdot\boldsymbol{v} - \lambda\nabla T], \tag{2.15}$$

where λ is the thermal conductivity. With these hydrodynamic equations including the gradient contributions, the entropy density $\hat{S}$ in Eq. (2.1) obeys

$$\frac{\partial\hat{S}}{\partial t} + \nabla\cdot\left[\hat{S}\boldsymbol{v} - Cn(\nabla\cdot\boldsymbol{v})\nabla n - \frac{\lambda}{T}\nabla T\right] = \frac{\dot{\epsilon}_v + \dot{\epsilon}_\theta}{T}, \tag{2.16}$$

where the right-hand side is the non-negative-definite entropy production rate with

$$\dot{\epsilon}_v = \sum_{ij}\sigma_{ij}\nabla_j v_i, \quad \epsilon_\theta = \lambda(\nabla T)^2/T. \tag{2.17}$$

In passing, the constant s_0 in Eq. (2.4) may be omitted in Eq. (2.16) owing to the continuity equation (2.11).

C. Boundary conditions

We assume the no-slip boundary condition,

$$\boldsymbol{v} = \boldsymbol{0}, \tag{2.18}$$

on all the boundaries for simplicity. However, a number of molecular-dynamics simulations have shown that a slip of the fluid velocity tangential to the wall becomes significant around a moving contact line [57]. On the basis of their molecular-dynamics simulation [58], Qian *et al.* proposed to use a generalized Navier boundary condition on a solid boundary in the continuum limit. In our work, even under the no-slip boundary condition, a significant velocity field is induced around a contact line [28] or an advancing film edge.

We assume the surface entropy density $\sigma_s(n_s)$ and the surface energy density $e_s(n_s)$ depending on the fluid density at the surface, written as n_s. The total entropy including the surface contribution is of the form

$$\mathcal{S}_{\mathrm{tot}} = \int d\boldsymbol{r}\hat{S} + \int da\sigma_s, \tag{2.19}$$

where $\int da$ is the surface integral over the boundaries. The total fluid energy is given by

$$\mathcal{E}_{\mathrm{tot}} = \int d\boldsymbol{r}\left(e + \tfrac{1}{2}\rho\boldsymbol{v}^2 + \rho U\right) + \int da e_s. \tag{2.20}$$

We assume that there is no strong adsorption of the fluid particles onto the boundary walls. The fluid density is continuously connected from the bulk to the boundary surfaces; for example, we have $n_s(x,y,t)=\lim_{z\to+0} n(\boldsymbol{r},t)$ at $z=0$. Then the total particle number of the fluid in the cell is the bulk integral $\mathcal{N}=\int d\boldsymbol{r}n$.

We assume that the temperatures in the fluid and in the solid are continuously connected at the surfaces. The temperature on the substrate is then well defined and we may introduce the surface Helmholtz free-energy density

$$f_s = e_s - T\sigma_s. \tag{2.21}$$

As the surface boundary condition, we require

$$C\hat{\boldsymbol{\nu}}_b\cdot\nabla n = \frac{-1}{T}\left(\frac{\partial f_s}{\partial n_s}\right)_T, \tag{2.22}$$

where $\hat{\boldsymbol{\nu}}_b$ is the outward surface normal unit vector. In the literature [1], this boundary condition is obtained in equilibrium with homogeneous T by minimization of the total Helmholtz (Ginzburg-Landau) free energy,

$$F_{\mathrm{tot}} = \int d\boldsymbol{r}(e - T\hat{S}) + \int da f_s. \tag{2.23}$$

We assume the boundary condition (2.22) even in nonequilibrium, while using F_{tot} in the bulk region with inhomogeneous temperature is not appropriate. The use of Eqs. (2.16), (2.19), and (2.22) now yields the total entropy increasing rate in our theory [55],

$$\frac{d}{dt}\mathcal{S}_{\mathrm{tot}} = \int d\boldsymbol{r}\frac{\dot{\epsilon}_v + \dot{\epsilon}_\theta}{T} + \int da\frac{\hat{\boldsymbol{\nu}}_b\cdot\lambda\nabla T + \dot{e}_s}{T}, \tag{2.24}$$

where $\dot{e}_s=\partial e_s/\partial t=(\partial e_s/\partial n_s)(\partial n_s/\partial t)$. The first term in the right-hand side is the bulk entropy production rate, while the second term is the surface integral of the heat flux from the solid divided by T or the entropy input from the solid to the bulk fluid.

In this paper, we present simulation results with $U=0$ for simplicity. In our previous work [49] a large gravity field was assumed in boiling. In future we should investigate the effect of the long-range van der Waals interaction in the wetting dynamics.

III. SIMULATION METHOD

In our phase field simulation, we integrated the continuity equation (2.11), the momentum equation (2.12), and the entropy equation (2.16), not using the energy equation (2.15), as in our previous simulation [28]. With this method, if there is no applied heat flow, temperature and velocity gradients tend to vanish at long times in the whole space including the interface region. This numerical stability is achieved because the heat production rate $\dot{\epsilon}_v+\dot{\epsilon}_\theta \geq 0$ appears explicitly in the entropy equation, so that $d\mathcal{S}_{\rm tot}/dt \geq 0$ in Eq. (2.24) without applied heat flow. We then obtain smooth variations of the temperature and velocity near the film edge (those around the contact line of an evaporating droplet in Ref. [28]).

It is worth noting that many authors have encountered a parasitic flow around a curved interface in numerically solving the hydrodynamic equations in two-phase states [52,59]. It remains nonvanishing even when the system should tend to equilibrium without applied heat flow. It is an artificial flow since its magnitude depends on the discretization method.

A. Fluid in a cylindrical cell

We suppose a cylindrical cell. Our model fluid is in the region $0 \leq z \leq H$ and $0 \leq r=(x^2+y^2)^{1/2} \leq L$, where $H=300\Delta x$ and $L=400\Delta x$ with Δx being the simulation mesh length. The velocity field $\boldsymbol{v}$ vanishes on all the boundaries. In this axisymmetric geometry, all the variables are assumed to depend only on z, r, and t. The integration of the dynamic equations is on a 200×400 lattice in the fluid region. We set $\Delta x=\ell/2$, where ℓ is defined in Eq. (2.8). We will measure space in units of ℓ. Then $H=150$ and $L=200$ in units of ℓ.

The transport coefficients are proportional to n as

$$\eta=\zeta=\nu_0 mn, \quad \lambda=k_B\nu_0 n. \tag{3.1}$$

These coefficients are larger in liquid than in gas by the density ratio n_ℓ/n_g (~ 5 in our simulation). The kinematic viscosity $\nu_0=\eta/mn$ is a constant. We will measure time in units of the viscous relaxation time,

$$\tau_0=\ell^2/\nu_0=C/2k_B\upsilon_0\nu_0, \tag{3.2}$$

on the scale of ℓ. The time mesh size of our simulation is $\Delta t=0.01\tau_0$. Away from the criticality, the thermal diffusivity $D_T=\lambda/C_p$ is of order ν_0 and the Prandtl number $Pr=\nu_0/D_T$ is of order unity, so τ_0 is also the thermal relaxation time on the scale of ℓ. Here, the isobaric specific heat C_p per unit volume is of order n far from the criticality, while it grows in its vicinity. With Eq. (3.1), there arises a dimensionless number given by

$$\sigma=m\nu_0^2/\epsilon\ell^2=m\ell^2/\epsilon\tau_0^2. \tag{3.3}$$

The transport coefficients are proportional to $\nu_0 \propto \sigma^{1/2}$. For He^3, for example, the critical temperature is $T_c=3.32$ K and, by setting $\epsilon=27k_BT_c/8$ from Eq. (2.7), we have $\sigma^{1/2}\ell=\nu_0(m/\epsilon)^{1/2}=2.03\times 10^{-8}$ cm near the gas-liquid critical point. In this paper we set $\sigma=0.06$, for which sound waves are well defined as oscillatory modes for wavelengths longer than ℓ (see Fig. 6) [49].

We will measure velocities in units of $\ell/\tau_0=\nu_0/\ell$. Another velocity unit is the capillary velocity γ/η with η being the liquid viscosity. At $T=0.875T_c$, the surface tension γ is calculated as

$$\gamma=0.082k_BT_c\ell/\upsilon_0=0.66p_c\ell. \tag{3.4}$$

Using Eqs. (3.1) and (3.2) and setting $\sigma=0.06$ we find $\gamma/\eta \sim 0.03\ell/\sigma\tau_0 \sim 0.5\ell/\tau_0$. These velocity units are of the same order, much exceeding the film speed and the gas velocity near the film edge (discussions regarding Fig. 4).

The temperature at the top $z=H$ is fixed at T_H, while the sidewall at $r=L$ is thermally insulating or $\hat{\boldsymbol{\nu}}_b\cdot\nabla T=\partial T/\partial r=0$ at $r=L$. As the boundary condition of the density, we set $\partial n/\partial z=0$ on the top plate at $z=H$ and $\partial n/\partial r=0$ on the sidewall at $r=L$. On the substrate $z=0$, it is given by

$$\upsilon_0\ell\frac{\partial n}{\partial z}=-\Phi_1, \tag{3.5}$$

where Φ_1 arises from the short-range interaction between the fluid and the solid wall [1,45]. From Eqs. (2.19)–(2.22) this can be the case if $e_s=$const and $\sigma_s=(\Phi_1 C/\upsilon_0\ell)n_s+$const, where the constant terms are independent of n. We treat Φ_1 as a parameter independent of T around $T=0.875T_c$. For example, at $T=0.875T_c$, the contact angle θ is $\pi/2$ at $\Phi_1=0$, 0.32π at $\Phi_1=0.05$ [28], and zero at $\Phi_1=\Phi_{1c}\cong 0.06$. The wall is completely wetted by liquid for $\Phi_1>\Phi_{1c}$ in equilibrium.

B. Solid substrate

In our previous work, we assumed a constant temperature at the bottom plate $z=0$ [28,48,49]. In this paper, we suppose the presence of a sold wall in the region $-H_{\rm w} \leq z \leq 0$ and $0 \leq r=(x^2+y^2)^{1/2} \leq L$, where its thickness is $H_{\rm w}=100\Delta x=50\ell=H/3$. The temperature in the solid obeys the thermal diffusion equation

$$C_{\rm w}\frac{\partial T}{\partial t}=\lambda_{\rm w}\nabla^2 T, \tag{3.6}$$

where $C_{\rm w}$ is the heat capacity (per unit volume) and $\lambda_{\rm w}$ is the thermal conductivity of the solid. The temperature $T(r,z,t)$ is continuous across the substrate $z=0$. In our simulation, the thermal diffusivity in the solid is given by $D_{\rm w}=\lambda_{\rm w}/C_{\rm w}=400\nu_0$, while the thermal diffusivity of the fluid D_T is of order ν_0 away from the criticality. Thus, the thermal relaxation time in the substrate is $H_{\rm w}^2/D_{\rm w}=25\tau_0$, which is shorter than typical spreading times to follow. Because $D_{\rm w} \gg D_T$, we integrated Eq. (3.6) using the implicit Crank-Nicolson method on a 100×400 lattice.

In this paper, the temperature T at the substrate bottom $z=-H_{\rm w}$ is held fixed at a constant $T_{\rm w}$. That is, for any r, we assume

$$T(r,-H_w)=T_w. \tag{3.7}$$

Heating (cooling) of the fluid occurs when T_w is higher (lower) than the initial fluid temperature T_0. There is no heat flux through the sidewall, so $\partial T/\partial r=0$ at $r=L$ as in the fluid region. From the energy conservation at the boundary, the heat flux on the substrate surface is continuous as

$$(\lambda_w T')_{z=-0}=(\lambda T')_{z=+0}, \tag{3.8}$$

where $T'=\partial T/\partial z$. This holds if there is no appreciable variation of the surface energy density e_s. We define the parameter

$$\Lambda=\lambda/(n v_0 \lambda_w)=k_B \nu_0/v_0 \lambda_w. \tag{3.9}$$

Then $(T')_{z=-0}=\Lambda n_s v_0 (T')_{z=+0}$ on the substrate. In this paper, Λ is set equal to 0.002 or 0.2. We found that the boundary temperature at $z=0$ is nearly isothermal at $T=T_w$ for $\Lambda=0.002$ but considerably inhomogeneous around the edge for $\Lambda=0.2$ (see Figs. 4, 5, and 8 below).

C. Preparation of the initial state and weak adsorption pre-existing before spreading

To prepare the initial state, we first placed a semispheric liquid droplet with radius $R=40\ell$ on the substrate $z=0$ with gas surrounding it. Here, we set $\Phi_1=0$ to suppress adsorption of the fluid to the solid. The temperature and pressure were $T=T_0=0.875T_c$ and $p=p_{cx}(T_0)=0.573p_c$ on the coexistence line in the fluid. The liquid and gas densities were those on the coexistence curve, $n_\ell^0=0.579v_0^{-1}$ in liquid and $n_g^0=0.123v_0^{-1}$ in gas. The entropy difference between the two phases is $2.1k_B$ per particle. The total particle number is $N=2\pi(n_\ell^0-n_g^0)R^3/3+\pi n_g^0 L^2 H=1.61\times 10^6 \ell^3/v_0$. The particle number in the droplet is about 5% of N.

Next, we waited for an equilibration time of 10^4 with $\Phi_1=0$. The contact angle θ was kept at $\pi/2$ and $\hat{\boldsymbol{\nu}}_b\cdot\nabla n=0$ on all the boundary surfaces. As will be shown in the Appendix, the liquid and gas pressures were slightly changed to $0.608p_c$ and $0.575p_c$, respectively. The pressure difference $\Delta p=0.033p_c$ is equal to $2\gamma/R$ from the Laplace law, where γ is in Eq. (3.4). As a result, the liquid density was increased to $0.583v_0^{-1}$ and the droplet radius was decreased to 38ℓ. Thus, the fluid nearly reached equilibrium with $\theta=\pi/2$ or without excess boundary adsorption. After this equilibration we hereafter set $t=0$ as the origin of the time axis.

At $t=0$, we changed the wetting parameter Φ_1 in the boundary condition (3.5) from 0 to 0.061 to realize the complete wetting condition. Before appreciable spreading, weak adsorption of the fluid has been induced on the substrate in a short time of order unity (in units of τ_0). For small Φ_1 and away from the contact line, this pre-existing density deviation, written as $\delta n(z)$, is of the exponential form

$$\delta n(z)=(\xi\Phi_1/v_0\ell)e^{-z/\xi}, \tag{3.10}$$

in terms of the correlation length ξ. Note that homogeneity of $\hat{\mu}$ in Eq. (2.3) yields $(\xi^{-2}-\partial^2/\partial z^2)\delta n=0$ in the linear order, leading to Eq. (3.10) under Eq. (3.5). The z integration of $\delta n(z)$ is the excess adsorption

$$\Gamma_{ad}=\xi^2\Phi_1/v_0\ell. \tag{3.11}$$

In the gas at $T=0.875T_c$, Eq. (2.9) gives $\xi=1.68\ell$, leading to $\Gamma_{ad}=0.24\ell/v_0$. We shall see that this pre-existing adsorption is one order of magnitude smaller than that due to a precursor film ($\sim 2.5\ell/v_0$ in Fig. 6 below).

IV. SPREADING ON A COOLED SUBSTRATE

We present numerical results of spreading on a cooler substrate after the change of Φ_1. In one case, the bottom temperature T_w at $z=-H_w$ was lowered at $t=0$ from $T_0=0.875T_c$ to $0.870T_c$. In the other case, we kept $T_w=T_0$ even for $t>0$. The top temperature at $z=H$ was unchanged from T_0. Subsequently, spreading occurred with an increase in the liquid fraction due to condensation from gas to a precursor film. The fluid temperature near the film edge became significantly higher than the substrate temperature in these cases.

However, ahead of the film, a new liquid region (a ring in our geometry) appeared on the substrate for slightly deeper cooling (say, for $T_w=0.868T_c$) or for slightly larger Φ_1 (say, for $\Phi_1=0.065$). Such dew nucleation is another problem beyond the scope of this paper [60].

A. Evolution on long and short time scales

We first examine spreading in the cooled case $T_w=0.870T_c<T_0$ for $\Lambda=0.002$ and 0.2. In the early stage, strong disturbances are induced around the contact line, as in the case of droplet heating in the partial wetting condition [28]. For example, at $t=25$, the maximum gas velocity is $v_g=0.089$ and the contact line velocity is 0.14 for $\Lambda=0.2$. For $t\gtrsim 200$, a precursor film becomes well defined with reduced typical velocities.

Figure 1 displays droplet shapes in later times $t\gtrsim 500$ for $\Lambda=0.002$ and 0.2, where the liquid is divided into the droplet body in the region $r<r_{th}$ and the precursor film in the region $r_{th}<r<r_e(t)$. While $r_e(t)$ increases in time, r_{th} is nearly pinned around $52.5\ell=0.26L$. In our simulation, this pinning occurred for $t\gtrsim 200$. The film thickness ℓ_f also only weakly depends on time being about 5ℓ for $\Lambda=0.02$ and 0.2 (see the film profiles in Fig. 6 below). From the droplet profile around $r=r_{th}$ the apparent contact angle θ_{ap} decreases in time roughly as t^{-b} with $b\sim 0.7$ for $20\lesssim t\lesssim 3\times 10^3$. However, considerable uncertainties arise in the definitions of r_{th} and θ_{ap} since the droplet height ($\sim r_{th}\theta_{ap}$) approaches ℓ_f for our small droplet. On the other hand, in the previous experiments on involatile droplets [4–6,8], the droplet radius R was relatively large such that the droplet volume much exceeded the volume of a (possible) precursor film. As regard the droplet body, they confirmed Tanner's law derived from hydrodynamics [4] (the droplet radius increases slowly as $R\sim t^\alpha$ with $\alpha\sim 0.1$ and the apparent contact angle decreases as $\theta_{ap}\sim t^{-\beta}$ with $\beta\sim 0.3$).

Figure 2 gives the edge position $r_e(t)$ and the particle number in the total liquid region $N_\ell(t)$ as functions of time t for $\Lambda=0.2$ in the cooled case with $T_w=0.870T_c$ and in the noncooled case with $T_w=T_0=0.875T_c$. In the early stage, $r_e(t)$ represents the droplet edge starting with the initial drop-

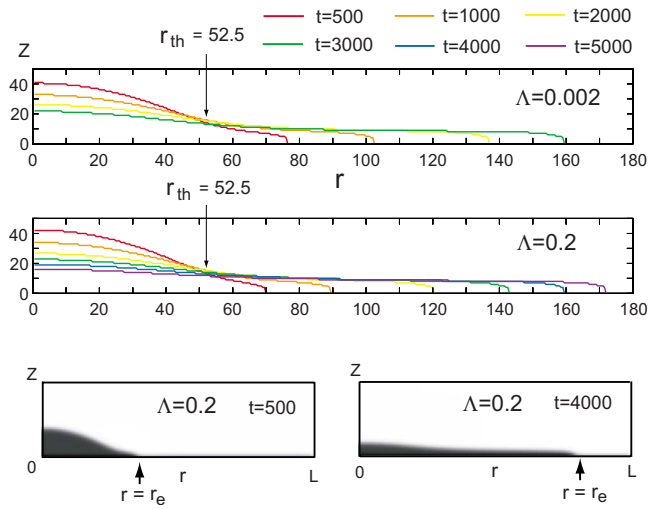

FIG. 1. (Color online) Shapes of an axisymmetric small droplet spreading on a cooler substrate with $T_w=0.870T_c$ at various times ($t\geq 500$) for $\Lambda=0.002$ (top) and 0.2 (middle) in the r-z plane. The system temperature was initially $T_0=0.875T_c$ at $t=0$. The boundary position between the main body of the droplet and the precursor film is fixed at $r=r_{th}=52.5\ell$ at these times for $\Lambda=0.02$ and 0.2. The edge position $r_e(t)$ of the film increases with time as illustrated in the bottom plates.

let radius (=38). It exceeds $r_{th}=52.5$ for $t>170$. In these cooled and noncooled cases, $r_e(t)$ and $N_\ell(t)$ grow in time due to condensation. We calculate $N_\ell(t)$ from

$$N_\ell(t)=2\pi\int_0^{r_e(t)}drr\int_0^{z_{\rm int}(r,t)}dzn(\boldsymbol{r},t), \tag{4.1}$$

where the interface height is at $z=z_{\rm int}(r,t)$ in the range $0<r<r_e(t)$. $z_{\rm int}(r,t)$ is determined by

$$n(r,z_{\rm int},t)=(n_\ell^0+n_g^0)/2, \tag{4.2}$$

where $n_\ell^0=0.579v_0^{-1}$ and $n_g^0=0.123v_0^{-1}$ are the densities on the coexistence curve at $T=0.875T_c$. In our case, the film is so

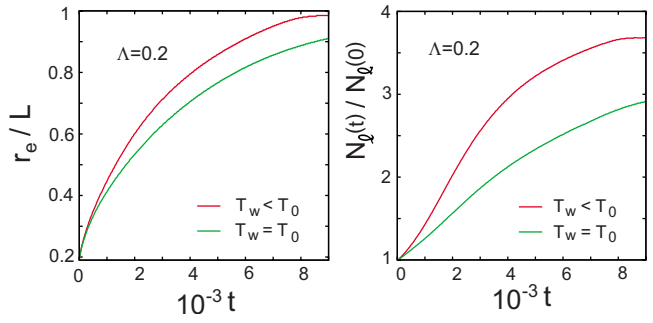

FIG. 2. (Color online) Time evolutions of the edge position $r_e(t)$ divided by L (left) and the particle number in the droplet $N_\ell(t)$ divided by $N_\ell(0)$ (right) for $\Lambda=0.2$. The upper curve corresponds to $T_w=0.870T_c<T_0$ (red), while the lower one corresponds to $T_w=0.875T_c=T_0$ (green). The interface curve is determined by Eq. (4.2). The film edge reaches the sidewall at $t\sim 10^4$. Condensation occurs faster in the cooled case $T_w<T_0$ than in the noncooled case $T_w=T_0$.

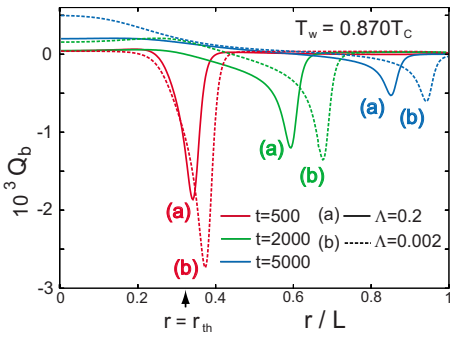

FIG. 3. (Color online) Heat flux on the substrate $Q_b(r,t)$ as a function of r in units of $\epsilon\ell/v_0\tau_0$ for $T_w=0.870T_c<T_0$ with $\Lambda=0.002$ and 0.2 at $t=500$ (left), 2000 (middle), and 5000 (right). A negative peak at the film edge indicates transport of latent heat from the fluid to the solid. At long times this absorption becomes weaker and there appears a heat flow from the solid to the fluid for $r<r_{th}$.

thin and there is no unique definition of $z_{\rm int}$. Then $N_\ell(t)$ starts from the initial number $N_\ell(0)=0.67\times 10^5\ell^3/v_0$ and becomes a few times larger at $t\sim 10^4$. In the time region $20\lesssim t\lesssim 3\times 10^3$, we roughly obtain

$$r_e(t)-r_e(0)\sim t^{0.6},\quad N_\ell(t)-N_\ell(0)\sim t^{1.1}, \tag{4.3}$$

both for $T_w/T_c=0.870$ and 0.875. For $t\lesssim 20$, dr_r/dt and the maximum gas velocity are of order 0.1.

In Fig. 3, we display the heat flux on the substrate $Q_b(r,t)$ for the same runs. From Eq. (3.8) it is defined in terms of the temperature gradient $T'=\partial T/\partial z$ as

$$Q_b(r,t)=-(\lambda_w T')_{z=-0}=-(\lambda T')_{z=+0}. \tag{4.4}$$

Negative peaks indicate absorption of latent heat from the fluid to the substrate around the film edge. However, at long times ($t=5\times 10^3$ in the figure) heat is from the solid to the fluid in the region of the droplet body $r<r_{th}$. The amplitude of $Q_b(r,t)$ around the peak is larger for $\Lambda=0.002$ than for $\Lambda=0.2$, obviously because heat is more quickly transported for smaller Λ or for larger λ_w. Also $Q_b(r,t)$ is sensitive to T_0-T_w. For example, in the noncooled case $T_w=T_0$, the minima of $Q_b(r,t)$ became about half of those in Fig. 3 (not shown here). In our previous simulation [28], a positive peak of $Q_b(r,t)$ was found at the contact line of an evaporating droplet.

In Fig. 4, we present the temperature near the edge at $t=10^3$ in color in the upper panel and the substrate temperature at $z=0$ in the lower panel, where $\Lambda=0.2$ and $T_w=0.870T_c<T_0$. The fluid temperature exhibits a hot spot in the gas side produced by latent heat. The substrate temperature is maximum at the film edge. Such a temperature variation in the solid should be measurable [31]. In this run, the peak height of the hot spot is $(T_p-T_w)/T_c=0.01$. At $t=10^3$, the maximum gas velocity is $v_g=0.014$ around the hot spot, while the mean velocity in the film near the edge is of order 0.01. The corresponding Reynolds number $v_g\ell_f/\nu_0$ in the gas is small ($\sim$0.07 here). Surprisingly, the fastest velocity is the edge speed $dr_e/dt=0.04$ in this case. It is possible when the film expands due to condensation near the film edge. On the

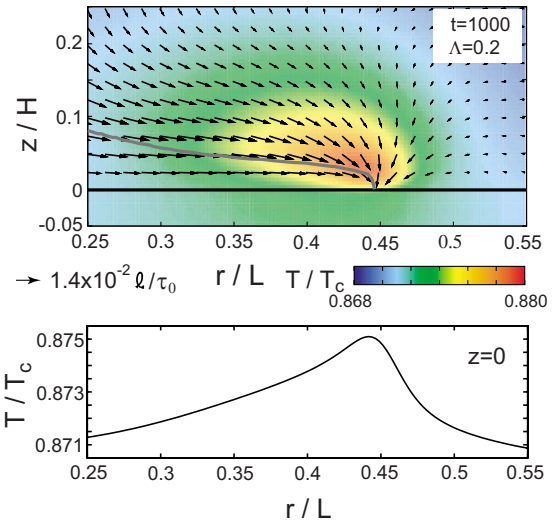

FIG. 4. (Color online) Temperature T around an advancing film edge at $t=10^3$, where $T_w=0.870T_c$ and $\Lambda=0.2$. In the top, the color represents the temperature according to the color map, and the velocity field is shown by arrows with its maximum being $1.4\times10^{-2}\ell/\tau_0$. In the bottom, the substrate temperature at $z=0$ is plotted, which is maximum at the edge position due to a finite thermal conductivity of the solid.

other hand, in the noncooled case $T_w=T_0$, the peak height was reduced to $T_p-T_0=0.007T_c$ and v_g to 0.008 at $t=10^3$.

In Fig. 5, we show time evolution of the temperature maxima, denoted by T_p and T_{sp}, in the fluid and on the substrate at $z=0$, respectively, in the cooled case $T_w=0.870T_c$ for $\Lambda=0.2$ and 0.002. The maxima are at the contact line right after the cooling and near the film edge after the precursor film formation. The substrate temperature also exhibits a smaller peak for $\Lambda=0.2$, but it becomes nearly homogeneous for $\Lambda=0.002$.

In Fig. 6, we display time evolution of the pressure and the temperature at the position $(z,r)=(0.48H,0.5L)$ in the

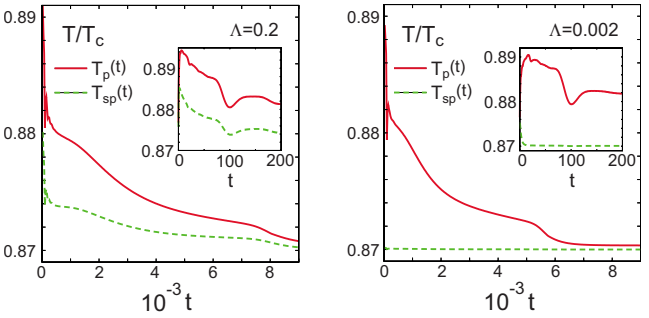

FIG. 5. (Color online) Maxima of the fluid temperature $T_p(t)$ (upper curve) and the substrate temperature $T_{sp}(t)$ (lower curve) vs time t in the cooled case $T_w=0.870T_c$ with $\Lambda=0.2$ (left) and $\Lambda=0.002$ (right). T_p is the temperature at the hot spot after formation of a precursor film, while it is the temperature at the contact line at short times. Peak height $T_{sp}-T_w$ on the substrate is still significant for $\Lambda=0.2$ but is nearly zero for $\Lambda=0.002$. Insets: behavior of T_p and T_{sp} in an early stage, where minima are produced by a low-pressure acoustic pulse reflected from the upper boundary (see the insets of Fig. 6).

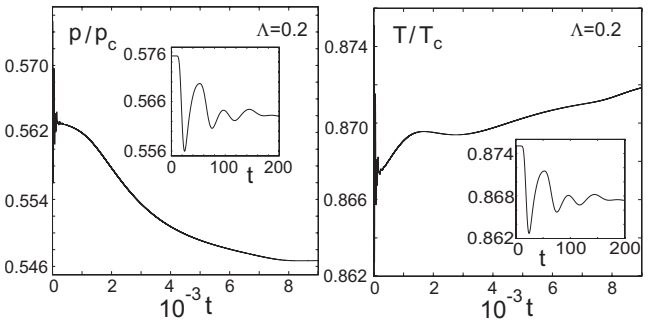

FIG. 6. Pressure (left) and temperature (right) vs t at the point $(z/H,r/L)=(0.48,0.5)$ far from the substrate in gas, where $T_w=0.870T_c$ and $\Lambda=0.2$. Their short-time behavior ($t<200$) is due to propagation of a low-pressure sound pulse in the cell and is adiabatic (inset), while their long-time behavior is due to gradual condensation.

gas region far from the substrate in the cooled case $T_w=0.870T_c$ with $\Lambda=0.2$. In the inset, their initial deviations originate from a lower-pressure sound pulse emitted from the adsorption layer in Eq. (3.10). This acoustic process is an example of the piston effect [61,62]. In the present case, the thermal diffusion layer due to cooling of the substrate gives rise to a smaller effect. The emitted pulse traverses the cell on the acoustic time $H/c_g\sim50$ and is reflected at the top plate, where $c_g\sim4$ is the sound velocity in the gas. The first deep minima of T below T_w and that of p at $t\sim25$ are due to its first passage. Here, the adiabatic relation $\delta T=(\partial T/\partial p)_s\delta p$ is well satisfied for the deviations $\delta T=T-T_0$ and $\delta p=p-p_0$. The adiabatic coefficient $(\partial T/\partial p)_s$ is equal to $11T_c/p_c$ in the gas and is larger than that in the liquid by one order of magnitude. On long time scales, Fig. 6 shows that the pressure gradually decreases with progress of condensation, while the temperature increases for $200\lesssim t\lesssim1500$, slowly decreases for $1500\lesssim t\lesssim3000$, and again increases for longer t. The gas temperature in the middle region is slightly higher than T_w by $0.002T_c$ at $t=9\times10^3$. We note that the gas temperature is influenced by a gas flow from the droplet and behaves in a complicated manner.

B. Profiles of density, temperature, and pressure

Here, we introduce the normal pressure $\tilde{p}$ by

$$\tilde{p}=\sum_{ij}\hat{\nu}_i\hat{\nu}_j\Pi_{ij}=p-CT(n\nabla^2n-|\nabla n|^2/2), \qquad (4.5)$$

where Π_{ij} is the reversible stress tensor in Eq. (2.13), p is the van der Waals pressure in Eq. (2.6), and $\hat{\boldsymbol{\nu}}=\{\hat{\nu}_i\}=\{\nabla_i n/|\nabla n|\}$ is the unit vector along the density gradient ∇n. Obviously, $\tilde{p}\cong p$ in the bulk region. In equilibrium, $\tilde{p}$ is independent of space and is equal to the saturation pressure $p_{cx}(T)$ across a planar interface, while its deviation from $p_{cx}(T)$ is of order R^{-1} across a spherical interface with radius R^{-1} (see the Appendix). Even in nonequilibrium, we found that inhomogeneity of $\tilde{p}$ around an interface remains relatively weak (smaller than that of p by one order of magnitude).

In Fig. 7, we show the profiles of the density n, the temperature T, and the normal pressure $\tilde{p}$ along the density gra-

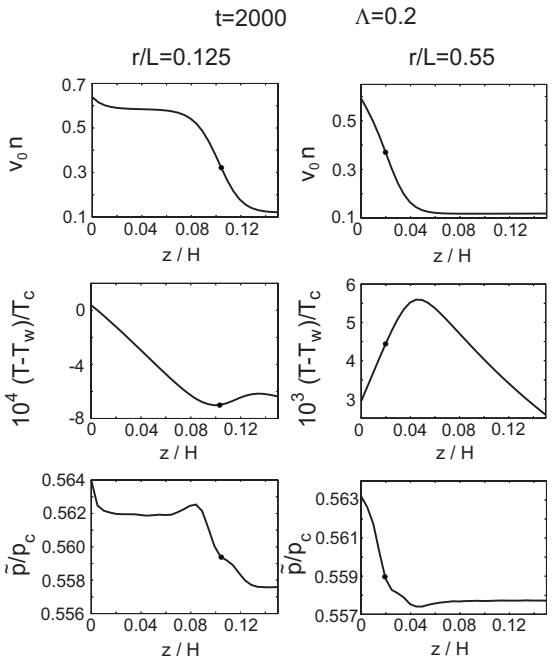

FIG. 7. Density (top), temperature (middle), and normal pressure (bottom) as functions of the distance z from the substrate at $r/L=0.125$ (left) and at $r/L=0.55$ (right) at $t=2\times10^3$, where $T_w=0.870T_c<T_0$ and $\Lambda=0.2$. The former path passes through the droplet body, while the latter passes through the film edge. The temperature peak is at $r/L=0.59$. Temperature variations are much smaller around the droplet body than around the film. The black dot (●) on each curve indicates the interface position determined by Eq. (4.2).

dient at $t=2\times10^3$ for $\Lambda=0.2$ and $T_w=0.870T_c$. In the left panels of Fig. 7 for $r=0.125L<r_{th}$, we can see weak adsorption near the wall in Eq. (3.10), a well-defined interface at $z\sim20$, and a small negative temperature gradient within the droplet body. For this r, a heat flow is weakly from the solid to the fluid. This is because the gas region above the droplet was initially cooled due to the piston effect, as Fig. 6 indicates. On the other hand, in the right panels for $r=0.55L>r_{th}$, n decreases from a liquid density near the wall to a gas density without a region of a flat density and T exhibits a peak. In this case, the hot peak is located at $r=0.59L$. The temperature variation around the film is larger than that in the droplet body by one order of magnitude. Furthermore, Fig. 8 gives a bird's eye view of the temperature near the edge from the same run, which corresponds to the middle right panel in Fig. 7. Here, the temperature inhomogeneity in the solid can also be seen.

It is of interest how the normal pressure and the temperature $(\tilde{p},T)$ at the interface is close to the coexistence line $(p_{cx}(T),T)$ in the p-T phase diagram. We define

$$h=\frac{T-T_0}{T_c}-\left(\frac{\partial T}{\partial p}\right)_{cx}\frac{\tilde{p}-p_0}{T_c}, \tag{4.6}$$

where the derivative $(\partial T/\partial p)_{cx}$ along the coexistence line is equal to $0.38T_c/p_c$ at $T=0.875T_c$. The upper panel of Fig. 9 displays h around the film at $t=10^3$, while the lower panel of

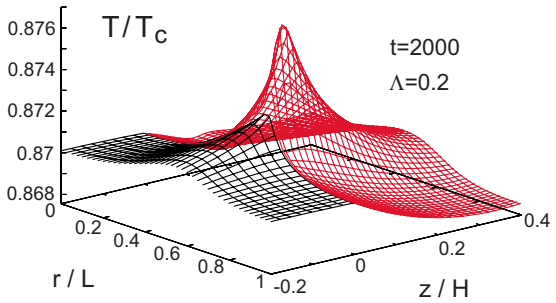

FIG. 8. (Color online) Temperature T around a film edge in the fluid $z>0$ (red) and in the solid $z<0$ (black) in the r-z plane at $t=2\times10^30$, where $T_w=0.870T_c$ and $\Lambda=0.2$. A peak is at $(r/L,z/H)=(0.59,0.035)$. See Fig. 4 for the hot spot at $t=10^3$ in color in the same run.

Fig. 9 gives h along the surface $z=z_{int}$ at four times for $\Lambda=0.2$ and 0.002. This quantity represents the distance from the coexistence line $p=p_{cx}(T)$ in the p-T phase diagram. In the bulk region, h is negative in stable liquid and metastable gas, while h is positive in stable gas and metastable liquid. We can see that h nearly vanishes in the droplet body in the region $r<r_{th}$ and increases in the film $r_{th}<r<r_e(t)$, but h remains less than 10^{-2} even at the edge. Note that the Laplace pressure contribution to h is $(\partial T/\partial p)_{cx}2\gamma/T_cR$, which is of order 0.01 in the droplet body $r<r_{th}$ at $t=10^3$.

C. Condensation rate and gas velocity

In our previous simulation [28], evaporation of a thick liquid droplet mostly takes place in the vicinity of the contact

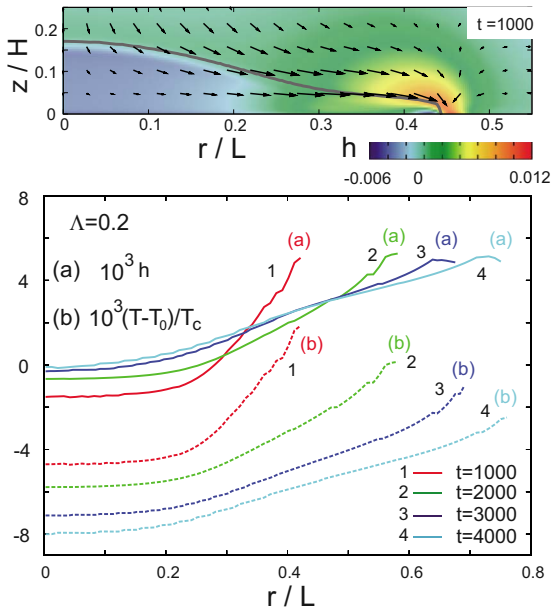

FIG. 9. (Color online) Top: distance from the coexistence line h in Eq. (4.6) at $t=10^3$ in color, which is negative in the droplet body and is positive in the film and in the gas. Here, $T_w=0.870T_c$ and $\Lambda=0.2$. Bottom: (a) h and (b) $(T-T_0)/T_c$ along the interface at $t=k\times10^3$ with $k=1$, 2, 3, and 4. For $r<r_{th}$, $|h|$ is much smaller than $(T_0-T)/T_c$, where local equilibrium holds. For $r>r_{th}=0.26L$, $|h|$ increases up to 4×10^{-3} with increasing r.

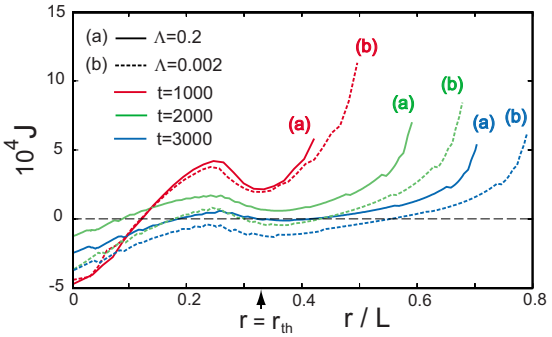

FIG. 10. (Color online) Flux $J(r,t)$ on the interface in units of $\ell/v_0\tau_0$ vs r/L in the region $0<r<r_e(t)$ at $t=10^3$ (left), 2×10^3 (middle), and 3×10^3 (right) for $T_w=0.870T_c$ in the two cases of $\Lambda=0.002$ and 0.2. A precursor film is on the left of the arrow. In its positive region J is the condensation rate. In its negative region $|J|$ is the evaporation rate.

line in the partial wetting condition. Here, we examine the space dependence of the condensation rate of a thin film in the complete wetting condition.

We introduce the number flux $J(r,t)$ from gas to liquid along $\hat{\boldsymbol{\nu}}=|\nabla n|^{-1}\nabla n$ through the interface,

$$J(r,t)=n(\boldsymbol{v}-\boldsymbol{v}_{int})\cdot\hat{\boldsymbol{\nu}}, \tag{4.7}$$

where $\boldsymbol{v}_{int}$ is the interface velocity. If J is regarded as a function of the coordinate along the normal direction $\hat{\boldsymbol{\nu}}$, it is continuous through the interface from the number conservation, while n and $\boldsymbol{v}\cdot\hat{\boldsymbol{\nu}}$ change discontinuously. Thus, we may well determine J on the interface. For $J>0$, it represents the local condensation rate. For $J<0$, $|J|$ represents the local evaporation rate. In Fig. 10, we plot $J(r,t)$ vs r/L in the region $0<r<r_e(t)$ at three times for $\Lambda=0.002$ and 0.2 in the cooled case $T_w=0.870T_c$. We recognize that $J(r,t)$ steeply increases in the precursor film and is maximum at the edge. Moreover, it becomes negative in the body part $r<r_{th}$ at $t=3\times10^3$, where evaporation occurs.

The total condensation rate $W_{tot}(t)$ is the surface integral of $J(r,t)$ on all the surface. The surface area in the range $[r,r+dr]$ is $da=2\pi drr/\sin\theta$, where θ is the angle between $\hat{\boldsymbol{\nu}}$ and the r axis. Thus,

$$W_{tot}(t)=2\pi\int_0^{r_e(t)}drrJ(r,t)/\sin\theta. \tag{4.8}$$

The particle number in the liquid region $N_\ell(t)$ in Eq. (4.1) increases in time as

$$\frac{d}{dt}N_\ell(t)=W_{tot}(t). \tag{4.9}$$

We also define the condensation rate in the film region,

$$W_{film}(t)=2\pi\int_{r_{th}}^{r_e(t)}drrJ(r,t)/\sin\theta, \tag{4.10}$$

where $\sin\theta\cong1$. In this integral the vicinity of the edge gives rise to a main contribution. In fact, the contribution from the region $r_e-16\ell<r<r_e$ is about 50% of the total contribution from the region $r_{th}<r<r_e$. Therefore, in terms of the gas velocity v_g and the gas density n_g around the edge, we estimate $W_{film}(t)$ as

$$W_{film}(t)\sim2\pi r_e n_g v_g \ell_c, \tag{4.11}$$

where ℓ_c is the width of the condensation area estimated to be about 30ℓ.

We introduce the number flux from the droplet body to the film at $r=r_{th}$ by

$$J_{flow}(t)=2\pi r_{th}\int_0^{z_{th}}dzn(r_{th},z,t)v_r(r_{th},z,t), \tag{4.12}$$

where $v_r(r,z,t)=v_x x/r+v_y y/r$ is the velocity in the plane within the film. In terms of the average density in the film $\bar{n}_\ell$ and the average fluid velocity $\bar{v}_\ell$ at $r=r_{th}$, we estimate

$$J_{flow}(t)\sim2\pi r_{th}\bar{n}_\ell\bar{v}_\ell. \tag{4.13}$$

More generally, we may introduce the flux

$$J_f(r,t)=2\pi r\int_0^{z_{th}}dzn(r,z,t)v_r(r,z,t), \tag{4.14}$$

for $r\geq r_{th}$ with z_{th} being the film thickness ℓ_f. In the presence of condensation onto the film, $J_f(r,t)$ increases from $J_f(r_{th},t)=J_{flow}(t)$ at $r=r_{th}$ with increasing r and reaches its maximum $J_f(r_e(t),t)$ at $r=r_e(t)$. For $\Lambda=0.2$, the ratio $J_f(r_e(t),t)/J_f(r_{th},t)$ was 1.1 at $t=10^3$ and 2.4 at $t=4\times10^3$.

We consider the particle number in the droplet body $N_b(t)$ and that in the precursor film $N_{film}(t)$. Here, $N_b(t)$ is the integral of $2\pi rJ(r,t)/\sin\theta$ in the region $r<r_{th}$ and $N_{film}(t)$ in the region $r_{th}<r<r_e$. Their sum $N_\ell(t)=N_b(t)+N_{film}(t)$ in Eq. (4.8) has been calculated in Fig. 2. In terms of $W_{tot}(t)$, $W_{film}(t)$, and $J_{flow}(t)$, they change in time as

$$\frac{d}{dt}N_b(t)=W_{tot}(t)-W_{film}(t)-J_{flow}(t), \tag{4.15}$$

$$\frac{d}{dt}N_{film}(t)=W_{film}(t)+J_{flow}(t). \tag{4.16}$$

Using the edge velocity $\dot{r}_e=dr_e/dt$, we also obtain

$$\frac{d}{dt}N_{film}(t)=2\pi r_e\dot{r}_e\bar{n}_\ell\ell_f, \tag{4.17}$$

since the film thickness is fixed in our case.

In Fig. 11, we plot $W_{tot}(t)$, $W_{film}(t)$, and $J_{flow}(t)$ vs t for $\Lambda=0.002$ and 0.2. In an early stage ($t<1.5\times10^3$ for $\Lambda=0.002$ and $t<2.6\times10^3$ for $\Lambda=0.2$), $W_{tot}(t)$ is larger than $W_{film}(t)$ and condensation occurs on all the interfaces. Afterward, the reverse relation $W_{tot}(t)<W_{film}(t)$ holds, where evaporation weakly occurs in the droplet body $r<r_{th}$. Moreover, $W_{film}(t)$ exceeds $J_{flow}(t)$ for $t\gtrsim10^3$ for these two values of Λ. Therefore, condensation near the film edge is the main mechanism of the precursor film growth except in the early stage [see the discussion below Eq. (4.10)], as speculated by Hardy [1,2]. In passing, let us estimate $W_{film}(t)$ and $J_{flow}(t)$ using Eqs. (4.11) and (4.13). For example, at $t=10^3$ (or 4×10^3) in the case $\Lambda=0.2$, the edge velocity is $\dot{r}_e=0.04$ (or 0.012), the gas velocity near the edge is $v_g=0.012$ (or

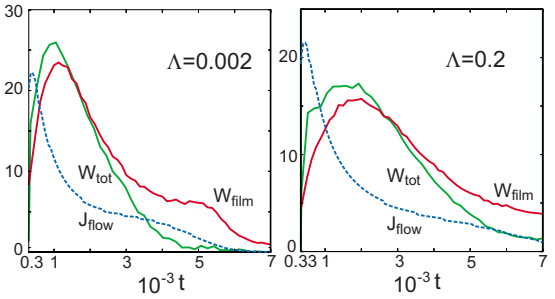

FIG. 11. (Color online) Total condensation rate $W_{\rm tot}(t)$ (green), condensation rate onto the film $W_{\rm film}(t)$ (red), and flow from the droplet body to the film $J_{\rm flow}(t)$ (blue) in units of $\ell^3/v_0\tau_0$ as functions of time. The time ranges are $[3\times10^2,7\times10^3]$ for $\Lambda=0.002$ (left) and $[3.3\times10^2,7\times10^3]$ for $\Lambda=0.2$ (right).

0.0064), and the fluid velocity at $r=r_{\rm th}$ is $\bar{v}_\ell=0.015$ (or 0.005). These values then yield $W_{\rm film}(t)\sim J_{\rm flow}(t)\sim 13$ at $t=10^3$ and $W_{\rm film}(t)\sim 3J_{\rm flow}(t)\sim 10$ at $t=4\times10^3$, in agreement with their curves in the right panel of Fig. 11.

In the left panel of Fig. 12, we plot the particle number in the droplet body $N_{\rm b}(t)=2\pi\int_0^{r_{\rm th}}drrJ(r,t)/\sin\theta$ for $\Lambda=0.2$ in the cooled case. Here, the upper bound $r_{\rm th}$ is longer than the real droplet radius on the substrate at short times $t\lesssim200$. Because of this definition, a small peak of $N_{\rm b}(t)$ arises at $t\sim200$ in Fig. 12. We confirmed that the numerical $N_{\rm b}(t)$ is consistent with the time integration of Eq. (4.15),

$$N_{\rm b}(t)-N_{\rm b}(0)=S_{\rm body}(t)-S_{\rm flow}(t). \tag{4.18}$$

In the right-hand side, the first term is the increase in the particle number due to condensation and evaporation expressed in the time integral

$$S_{\rm body}(t)=\int_0^t dt'[W_{\rm tot}(t')-W_{\rm film}(t')]. \tag{4.19}$$

The minims of the second term is the decrease in the particle number due to flow from the body into the film,

$$S_{\rm flow}(t)=\int_0^t dt' J_{\rm flow}(t'). \tag{4.20}$$

In the right panel of Fig. 12, $S_{\rm body}(t)$ and $S_{\rm flow}(t)$ are displayed for $\Lambda=0.2$ in the cooled case. We notice that $S_{\rm flow}(t)$

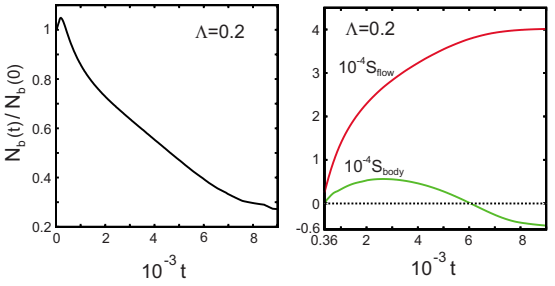

FIG. 12. (Color online) Left: particle number in the droplet body $N_{\rm b}(t)$ vs time t obeying Eq. (4.18). Right: $S_{\rm body}(t)$ in Eq. (4.19) (green) and $S_{\rm flow}(t)$ in Eq. (4.20) vs time t (red). $S_{\rm body}(t)$ is considerably smaller than $S_{\rm flow}(t)$ and its sign is changed at $t=6\times10^3$.

is considerably larger than $S_{\rm body}(t)$ and the droplet body shrinks mainly due to the flow from the body to the film, leading to $N_{\rm b}(0)-N_{\rm b}(t)\cong S_{\rm flow}(t)$. Since $S_{\rm body}(t)$ changes its sign, condensation dominates evaporation for $t<6\times10^3$ and vice versa at later times on the droplet body shrinkage.

We finally derive an approximate expression for the gas velocity v_g near the edge. The heat flux is of order $\lambda_\ell(T_{\rm p}-T_w)/\ell_f$ there, where $T_{\rm p}$ is the peak temperature and λ_ℓ is the liquid thermal conductivity. It balances with the convective latent heat flux $\sim n_gT_0\Delta s v_g$ in the gas, where n_g is the gas density and Δs is the entropy difference per particle. Therefore,

$$v_g\sim\lambda_\ell(T_{\rm p}-T_{\rm w})/(\ell_f n_gT_0\Delta s)\sim(T_{\rm p}-T_{\rm w})\bar{n}_\ell\nu_0/(T_0n_g\ell_f), \tag{4.21}$$

where we set $\lambda_\ell=k_B\nu_0\bar{n}_\ell$ and Δs $(=2.1k_B$ here) in the second line. Let us check the validity of the above estimate in our simulation. (i) In the upper plate of Fig. 4 at $t=10^3$ we have $v_g=0.014$, while the second line of Eq. (4.21) becomes a close value of 0.012 with $\ell_f/\ell\sim5$ and $\bar{n}_\ell/n_g\sim5$. (ii) From Eq. (4.21) the combination $v_g/(T_{\rm p}-T_{\rm w})$ should be a constant independent of time. In the cooled case $T_{\rm w}=0.870T_c$ with $\Lambda=0.2$, our data yield $v_gT_c/(T_{\rm p}-T_{\rm w})=2.48$, 1.49, 1.64, and 1.60 for $t=200$, 10^3, 2×10^3, and 4×10^3, respectively, so it is roughly equal to 1.6 in the late stage.

V. SPREADING AND EVAPORATION ON A HEATED SUBSTRATE

For $\Lambda=0.2$, we next present simulation results of a heated liquid droplet in the complete wetting condition, where $T_{\rm w}$ is increased above $T_0=0.875T_c$ at $t=0$. The other parameter values are the same as those in the previous section. The preparation method of a droplet is unchanged. Then a precursor film develops in an early stage (at least for small $T_{\rm w}-T_0$) because of the complete wetting condition at $\Phi_1=0.061$ [see Eq. (3.5)]. A new aspect is that evaporation dominates over condensation with increasing $T_{\rm w}-T_0>0$. The experiment by Guéna *et al.* [22] corresponds to this situation (see Sec. I).

The evaporation rate $-J$ (for negative J) from our simulation is very different from the phenomenological one $\propto[r_e(t)^2-r^2]^{-1/2}$ [24–26] as in Figs. 14 and 15 below. Also see Sec. I and Ref. [35] for this aspect.

A. Time evolution

In Fig. 13, we show the edge position $r_e(t)$ and the particle number in the liquid $N_\ell(t)$ as functions of t for three cases $T_{\rm w}=0.8855T_c$ [Fig. 13(a)], $T_{\rm w}=0.888T_c$ [Fig. 13(b)], and $T_{\rm w}=0.890T_c$ [Fig. 13(c)]. First, Fig. 13(a) is a special case, where the overall balance between condensation and evaporation is achieved at long times. That is, in Fig. 13(a), $r_e(t)$ and $N_\ell(t)$ tend to constants at long times and a steady thin pancakelike film is realized with radius $\sim0.5L$ and thickness $\sim4\ell$. Second, for higher $T_{\rm w}$, evaporation dominates over condensation and the liquid region eventually disappears at some time t_0. In other words, if $T_{\rm w}-T_0$ exceeds a critical value $(=0.0105T_c$ here), a liquid droplet has a finite

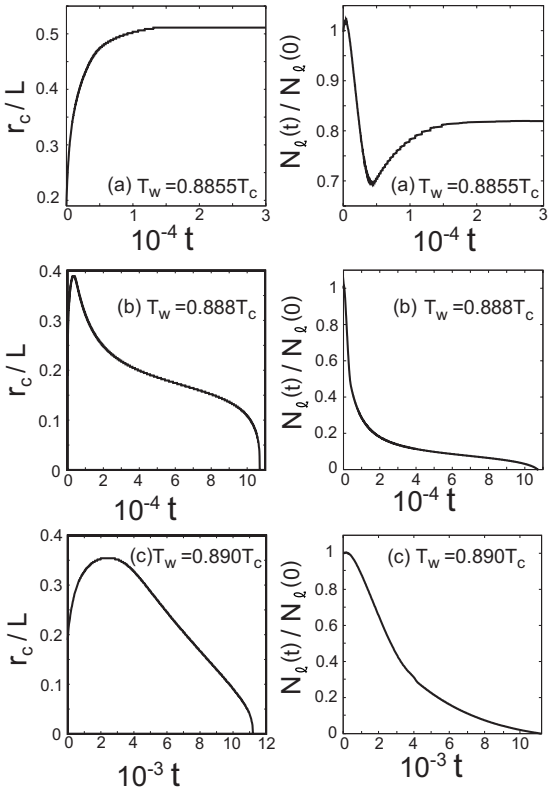

FIG. 13. Time evolutions of the edge position $r_e(t)$ divided by L (left) and the particle number in the droplet $N_\ell(t)$ divided by $N_\ell(0)$ (right) for $\Lambda=0.2$. The temperature T_w at the solid bottom was raised at $t=0$ from $0.875T_c$ to (a) $0.8855T_c$ (top), (b) $0.888T_c$ (middle), and (c) $0.890T_c$ (bottom). The fluid tends to a steady two-phase state in (a), where the liquid region assumes a pancake thin film. The liquid evaporates to vanish on a time scale of 10^5 in (b) and 10^4 in (c).

lifetime t_0 even in the complete wetting condition. The lifetime t_0 grows strongly as T_0-T_w approaches the critical value. In our examples, $t_0=1.07\times10^5$ for $T_w-T_0=0.018T_c$ in Fig. 13(b), while $t_0=1.12\times10^4$ for $T_w-T_0=0.020T_c$ in Fig. 13(c). As t approaches t_0, $r_e(t)$ may be fitted to the power-law form

$$r_e(t) \sim (t_0 - t)^c, \tag{5.1}$$

where $c\cong0.30$ in Fig. 13(b) and $c\cong0.43$ in Fig. 13(c). In our previous simulation of droplet evaporation in the partial wetting condition [28], this behavior was obtained with $c=0.42$. In experiments [22,24–27], macroscopic droplets evaporated in air obeying the power law with the classical exponent $c=0.5$.

B. Evaporation rate and temperature profile

In Fig. 14, we show the mass flux through the interface $J(r,t)$ defined in Eq. (4.7) in the weakly heated case (a) $T_w=0.8855T_c$. Its negativity implies evaporation. In the region far from the edge, evaporation is marked in transient states ($t\lesssim4\times10^3$), but it tends to vanish at long times. We can also see the region of positive J with width of order 10 near the edge ($r_e-10<r<r_e$), where the film is still flat and the angle

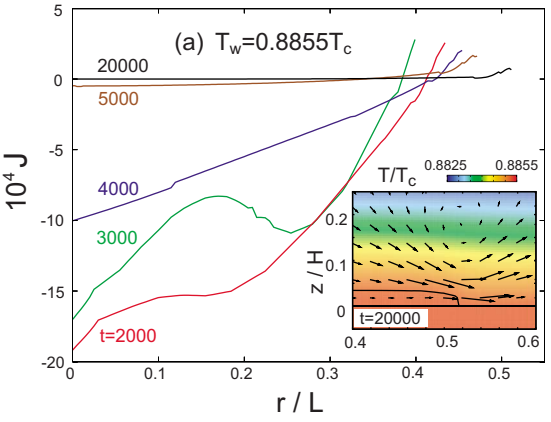

FIG. 14. (Color online) Mass flux $J(r,t)$ through the interface in Eq. (4.6) for the weakly heated case $T_w=0.8855T_c$ corresponding to (a) in Fig. 13. Evaporation takes place in the region $J<0$ except close to the edge. Here, J decreases in time. A steady two-phase state is approached at long times, where J is nonvanishing only near the edge. Inset: temperature in color and velocity represented by arrows at $t=2\times10^4$.

θ in Eq. (4.8) is nearly $\pi/2$. In Fig. 14, however, we do not show J just at the edge [$r\cong r_e(t)$ and $0<z<\ell_f$], where θ changes from $\pi/2$ to zero in the z direction and evaporation occurs ($J<0$). As a balance of condensation and evaporation in these two regions, the total condensation rate W_{tot} in Eq. (4.8) tends to vanish at long times, while there is no velocity field in the region $r<r_e-10$. In the inset of Fig. 14, the velocity field around the edge is displayed at $t=2\times10^3$, where the maximum gas velocity is $v_g=1.1\times10^{-3}\ell/\tau_0$.

In Fig. 15, we show $J(r,t)$ at several times in the highest heating case (c) $T_w=0.890T_c$. In the whole surface, J is negative and evaporation is taking place. For $t\lesssim4\times10^4$ evaporation is strongest at the film center, in sharp contrast to the case of a thick evaporating droplet [28]. At long times ($t=8\times10^3$ here), however, it becomes weakest at the film center. Figure 16 is produced by the same run. It gives a bird's eye view of the temperature in the upper panel and a snap-

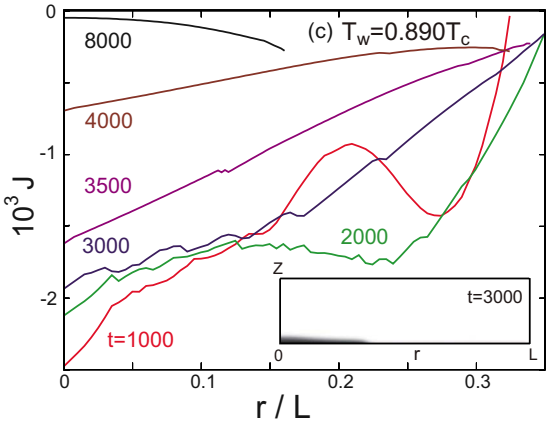

FIG. 15. (Color online) Mass flux through the interface $J(r,t)$ in Eq. (4.7) for the highest heating case $T_w=0.890T_c$ corresponding to (c) in Fig. 13. Here, evaporation takes place over the whole surface and the liquid disappears at $t=1.1\times10^4$. The inset displays the film shape at $t=3\times10^3$, where $N_\ell(t)$ is half of the initial value.

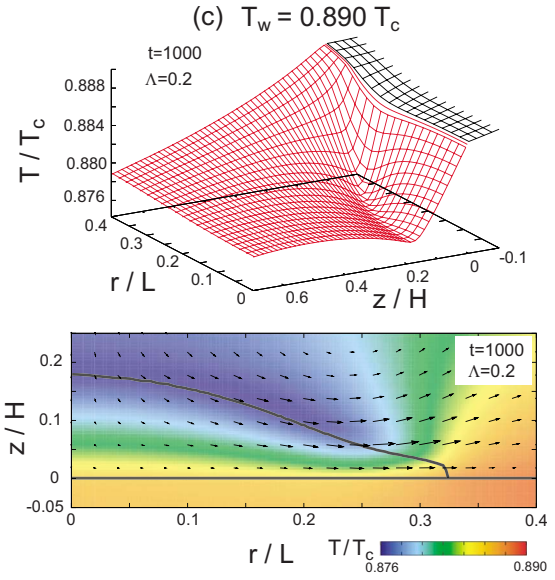

FIG. 16. (Color online) Top: temperature T in the region $0<r/L<0.4$ and $-0.1<z/H<0.7$ at $t=10^3$ in the highest heating $T_w=0.890T_c$ corresponding to (c) in Fig. 13. Bottom: temperature in color and velocity by arrows at the same time in the same run. A liquid film supports a large temperature gradient and evaporation occurs all over the surface, while the temperature above the film is nearly flat due to a gas flow. The maximum gas velocity is $v_g=0.024$.

shot of the velocity field in the vicinity of the film edge at $t=10^3$ in the lower panel. A similar bird's eye view of the temperature was presented for a thick evaporating droplet [28]. Remarkably, we can see a very steep temperature gradient within the film, which is much larger than in the gas, leading to a strong heat flux from the solid to the film. In this manner, evaporation is induced all over the surface and is strongest at the film center in the early stage. It is remarkable that the temperature gradient nearly vanishes in the gas region above the film away from the edge, where heat is transported by a gas flow. We also notice a significant temperature inhomogeneity in the solid part in contact with the film.

VI. SUMMARY AND REMARKS

For one-component fluids we have examined spreading of a small droplet on a smooth substrate in the complete wetting condition in the axisymmetric geometry. In the dynamic van der Waals theory [48,49], we have integrated the entropy equation in Eq. (2.16) together with the continuity and momentum equations. On the boundary walls, the velocity vanishes and the density derivative in the normal direction is a constant as in Eq. (3.5). This method may remove artificial flows around an interface [59]. In our phase field scheme, we need not introduce any interface boundary conditions. The condensation rate on the interface is a result and not a prerequisite of the calculation. We have also assumed that the substrate wall has a finite thickness H_w and the solid temperature obeys the thermal diffusion equation, whereas an isothermal substrate is usually assumed in the literature. The temperature T_w at the solid bottom $z=-H_w$ is a new control parameter in our simulation. Cooling (heating) the fluid is realized by setting T_w lower (higher) than the initial fluid temperature T_0. We give salient results in our simulation.

(i) In the cooled and noncooled cases with $T_w \leq T_0$, a precursor film with a constant thickness has appeared ahead of the droplet body. Here, the volume of the liquid region has increased in time due to condensation on the film as in Fig. 2, while that of the droplet body has decreased in time mainly due to flow from the body into the film as in Fig. 12. In a very early stage, the piston effect comes into play due to sound propagation [61,62]. At long times, the condensation rate has become localized near the film edge and the film has expanded due to condensation. As a result, a hot spot has appeared near the film edge because of the latent heat released.

(ii) At a critical value of T_w slightly higher than T_0, we have realized a steady-state thin liquid film, where condensation and evaporation are localized and balanced at the edge. For higher T_w, evaporation has dominated and the liquid region has disappeared eventually. This lifetime decreases with increasing T_w-T_0. For a thin film, evaporation has appeared all over the film surface upon heating. In our previous simulation for one-component fluids [28], on the other hand, evaporation of a thick droplet was mostly localized near the contact line in the partial wetting condition.

We give some critical remarks. (1) Our results cannot be directly compared with most of the previous experimental results on large involatile droplets such as Tanner's law. For our small droplet, the volume of the precursor film has exceeded the initial droplet volume in relatively short times ($\sim 10^3\tau_0$). We propose future experiments using volatile fluids to investigate a hot spot, for example. (2) If the mesh length $\Delta x=\ell/2$ is a few Å, our system length is on the order of several ten manometers and the particle number treated is of order 10^6 (see Sec. III C). Our continuum description should be imprecise on the angstrom scale. Thus, examination of our results by large-scale molecular-dynamics simulations should be informative. We should also investigate how our numerical results can be used or modified for much larger droplet sizes. (3) In future work, we should examine the role of the long-range van der Waals interaction in the wetting dynamics. As is well known, it crucially influences the film thickness [1]. (4) We should also include the slip effect at the contact line in our scheme [57,58]. (5) We should study the two-phase hydrodynamics in fluid mixtures, where a Marangoni flow decisively governs the dynamics even at small solute concentrations [25,29,34].

ACKNOWLEDGMENTS

We would like to thank Professor T. Qian for valuable discussions. This work was supported by Grants-in-Aid for scientific research on Priority Area "Soft Matter Physics" and the Global COE program "The Next Generation of Physics, Spun from Universality and Emergence" of Kyoto University from the Ministry of Education, Culture, Sports, Science and Technology of Japan. R.T. was supported by the Japan Society for Promotion of Science.

APPENDIX: EQUILIBRIUM TWO-PHASE COEXISTENCE

First we consider a planar interface at $z=0$ separating gas and liquid in equilibrium with a homogeneous T below T_c. Here, we may start with the Helmholtz free energy in Eq. (2.23) [54]. All the quantities change along the z axis. From the homogeneity of the generalized chemical $\hat{\mu}$ in Eq. (2.3) we obtain the equation for the interface density profile $n=n_{\rm in}(z)$ as

$$\mu(n_{\rm in}) - CTn''_{\rm in} = \mu_{\rm cx}, \tag{A1}$$

where $n''_{\rm in}=d^2n_{\rm in}/dz^2$ and $\mu_{\rm cx}$ is the equilibrium chemical potential in two-phase coexistence. We assume that $n_g=n_{\rm in}(\infty)$ is the gas density and $n_\ell=n_{\rm in}(-\infty)$ is the liquid density in equilibrium. The van der Waals pressure $p=p(n_{\rm in}(z))$ satisfies

$$p(n_{\rm in}) - CT[n_{\rm in}n''_{\rm in} - (n'_{\rm in})^2/2] = p_{\rm cx}, \tag{A2}$$

where $n'_{\rm in}=dn_{\rm in}/dz$ and $p_{\rm cx}$ is the equilibrium coexistence pressure. If differentiated with respect to z, the left-hand side of Eq. (A2) vanishes from Eq. (A1), ensuring its homogeneity. Notice that the left-hand side of Eq. (A2) is equal to $\tilde{p}$ in Eq. (4.5) or the zz component of the stress tensor. The van der Waals pressure $p(n_{\rm in})$ itself exhibits a large variation of order γ/ξ in the interface region. In fact, Eq. (A2) gives

$$\int dz[p(n_{\rm in}) - p_{\rm cx}] = -3\gamma/2. \tag{A3}$$

If use is made of Eq. (A1), this relation readily follows from the usual expressions for the surface tension [54],

$$\gamma = \int dz[f - \mu_{\rm cx}n + p_{\rm cx} + CT(n_{\rm in})^2/2] = \int dzCT(n'_{\rm in})^2, \tag{A4}$$

where $f=n\mu-p$ is the Helmholtz free-energy density.

Second, we consider a spherical liquid droplet with radius R in gas in equilibrium. The radius R is much longer than the interface thickness ξ. All the quantities depend only on the distance r from the droplet center. The homogeneity of $\hat{\mu}$ gives the equation of the density $n(r)$ as

$$\mu(n) - CT(n'' + 2n'/r) = \mu_{\rm cx} + \delta\mu_{\rm cx}, \tag{A5}$$

where $n'=dn/dr$, $n''=d^2n/dr^2$, and $\delta\mu_{\rm cx}$ is the correction arising from the curvature. For large R we set

$$n(r) = n_{\rm in}(r-R) + \delta n(r), \tag{A6}$$

where $\delta n \propto R^{-1}$. We may replace $2n'/r$ with $2n'/R$ in Eq. (A5). To linear order in the deviations we find

$$\left[\mu(n_{\rm in})' - CT\frac{d^2}{dr^2}\right]\delta n = \frac{2CT}{R}n'_{\rm in} + \delta\mu_{\rm cx}, \tag{A7}$$

where $\mu(n_{\rm in})'=(\partial\mu/\partial n)_T=1/n^2K_T$ at $n=n_{\rm in}$ with K_T being the compressibility. We multiply Eq. (A7) by $n'_{\rm in}$ and integrate both hand sides with respect to r across the interface to obtain

$$\delta\mu_{\rm cx}\Delta n = \Delta p = -2\gamma/R, \tag{A8}$$

where $\Delta n=n_g-n_\ell$ is the density difference. Here, we have used Eq. (A4) and the relation $\mu(n_{\rm in})'n'_{\rm in}-CTd^3n_{\rm in}/dz^3=0$. Thus, we have calculated the pressure difference between the two phases Δp and the chemical potential deviation $\delta\mu_{\rm cx}$ to linear order in R^{-1}. In the bulk gas and liquid regions far from the interface, δn tends to $(\delta n)_g$ in gas and $(\delta n)_\ell$ in liquid. From Eq. (A7) we obtain these bulk density deviations,

$$\mu'(n_g)(\delta n)_g = \mu'(n_\ell)(\delta n)_\ell = -2\gamma/R\Delta n. \tag{A9}$$

The bulk pressure deviations are

$$(\delta p)_g = -2n_g\gamma/R\Delta n, \quad (\delta p)_\ell = -2n_\ell\gamma/R\Delta n, \tag{A10}$$

in gas and in liquid, respectively. The deviation of the normal pressure $\tilde{p}$ in Eq. (4.5) from $p_{\rm cx}$ may also be expanded in powers of R^{-1}. To linear order we obtain

$$\delta\tilde{p} = \frac{2\gamma n_{\rm in}}{R\Delta n} + CT\left(\frac{2}{R}n_{\rm in}n''_{\rm in} - n''_{\rm in}\delta n + n'_{\rm in}\delta n'\right). \tag{A11}$$

In Fig. 7, the interface variation of $\delta\tilde{p}$ is smaller than that of $\delta p=p-p_{\rm cx}(\sim\gamma/\xi)$ by one order of magnitude.

[1] P. G. de Gennes, Rev. Mod. Phys. **57**, 827 (1985).
[2] W. Hardy, Philos. Mag. **38**, 49 (1919); see Ref. [1] for comments on this original work.
[3] V. E. Dussan, Annu. Rev. Fluid Mech. **11**, 371 (1979).
[4] L. H. Tanner, J. Phys. D **12**, 1473 (1979).
[5] J.-D. Chen, J. Colloid Interface Sci. **122**, 60 (1988).
[6] G. McHale, M. I. Newton, S. M. Rowan, and M. Banerjee, J. Phys. D **28**, 1925 (1995); in this paper, spreading of a stripe was studied.
[7] L. Leger and J. F. Joanny, Rep. Prog. Phys. **55**, 431 (1992).
[8] D. Bonn, J. Eggers, J. Indekeu, J. Meunier, and E. Rolley, Rev. Mod. Phys. **81**, 739 (2009).
[9] L. M. Hocking and A. D. Rivers, J. Fluid Mech. **121**, 425 (1982).
[10] D. Ausserré, A. M. Picard, and L. Léger, Phys. Rev. Lett. **57**, 2671 (1986).
[11] F. Heslot, A. M. Cazabat, and P. Levinson, Phys. Rev. Lett. **62**, 1286 (1989); F. Heslot, A. M. Cazabat, P. Levinson, and N. Fraysse, *ibid.* **65**, 599 (1990).
[12] D. Beaglehole, J. Phys. Chem. **93**, 893 (1989).
[13] H. P. Kavehpour, B. Ovryn, and G. H. McKinley, Phys. Rev. Lett. **91**, 196104 (2003).
[14] J.-X. Yang, J. Koplik, and J. R. Banavar, Phys. Rev. A **46**, 7738 (1992).
[15] J. A. Nieminen, D. B. Abraham, M. Karttunen, and K. Kaski, Phys. Rev. Lett. **69**, 124 (1992).
[16] T. Ala-Nissila, S. Herminghaus, T. Hjelt, and P. Leiderer, Phys. Rev. Lett. **76**, 4003 (1996); T. Hjelt, S. Herminghaus, T. Ala-Nissila, and S. C. Ying, Phys. Rev. E **57**, 1864 (1998).
[17] J. A. Nieminen and T. Ala-Nissila, Phys. Rev. E **49**, 4228

(1994); M. Haataja, J. A. Nieminen, and T. Ala-Nissila, *ibid.* **52**, R2165 (1995).
[18] J. De Coninck U. D'Ortona, J. Koplik, and J. R. Banavar, Phys. Rev. Lett. **74**, 928 (1995); U. D'Ortona, J. De Coninck, J. Koplik, and J. R. Banavar, Phys. Rev. E **53**, 562 (1996).
[19] J. Koplik, S. Pal, and J. R. Banavar, Phys. Rev. E **65**, 021504 (2002).
[20] A. Milchev and K. Binder, J. Chem. Phys. **116**, 7691 (2002); in this paper, Tanner's law was observed in a simulation of chainlike molecules.
[21] E. B. Webb III, G. S. Grest, and D. R. Heine, Phys. Rev. Lett. **91**, 236102 (2003).
[22] G. Guéna, C. Poulard, and A. M. Cazabat, J. Colloid Interface Sci. **312**, 164 (2007).
[23] J. Hegseth, A. Oprisan, Y. Garrabos, V. S. Nikolayev, C. Lecoutre-Chabot, and D. Beysens, Phys. Rev. E **72**, 031602 (2005).
[24] R. D. Deegan, O. Bakajin, T. F. Dupont, G. Huber, S. R. Nagel, and T. A. Witten, Nature (London) **389**, 827 (1997).
[25] H. Hu and R. G. Larson, Langmuir **21**, 3963 (2005); **21**, 3972 (2005).
[26] N. Shahidzadeh-Bonn, S. Rafai, A. Azouni, and D. Bonn, J. Fluid Mech. **549**, 307 (2006).
[27] H. J. Butt, D. S. Glovko, and E. Bonaccurso, J. Phys. Chem. B **111**, 5277 (2007).
[28] R. Teshigawara and A. Onuki, EPL **84**, 36003 (2008).
[29] J. Straub, Int. J. Therm. Sci. **39**, 490 (2000).
[30] V. S. Nikolayev, D. A. Beysens, G.-L. Lagier, and J. Hegseth, Int. J. Heat Mass Transfer **44**, 3499 (2001).
[31] C. Höhmann and P. Stephan, Exp. Therm. Fluid Sci. **26**, 157 (2002); in this boiling experiment, the substrate temperature exhibited a sharp drop by 0.2 K near a contact line in a narrow region of 10 μm length.
[32] D. Beysens, Y. Garrabos, V. S. Nikolayev, C. Lecoutre-Chabot, J.-P. Delville, and J. Hegseth, EPL **59**, 245 (2002).
[33] A. Onuki and K. Kanatani, Phys. Rev. E **72**, 066304 (2005).
[34] A. Onuki, Phys. Rev. E **79**, 046311 (2009).
[35] This phenomenological expression for $J(r)$ is not valid in evaporation in one-component fluids, where evaporation is much more localized near the contact line [28]. However, in the presence of air, the Marangoni effect can induce convection inside the droplet causing overall evaporation. This aspect should be further studied in the future.
[36] P. Ehrhard and S. H. Davis, J. Fluid Mech. **229**, 365 (1991); D. M. Anderson and S. H. Davis, Phys. Fluids **7**, 248 (1995).
[37] P. Seppecher, Int. J. Eng. Sci. **34**, 977 (1996).
[38] D. Jasnow and J. Viñals, Phys. Fluids **8**, 660 (1996); R. Chella and J. Viñals, Phys. Rev. E **53**, 3832 (1996).
[39] D. M. Anderson, G. B. McFadden, and A. A. Wheeler, Annu. Rev. Fluid Mech. **30**, 139 (1998).
[40] D. Jacqmin, J. Comput. Phys. **155**, 96 (1999).
[41] D. Jamet, O. Lebaigue, N. Coutris, and J. M. Delhaye, J. Comput. Phys. **169**, 624 (2001).
[42] R. Borcia and M. Bestehorn, Phys. Rev. E **67**, 066307 (2003); **75**, 056309 (2007).
[43] T. Araki and H. Tanaka, EPL **65**, 214 (2004).
[44] B. J. Palmer and D. R. Rector, Phys. Rev. E **61**, 5295 (2000); in an erratum to **69**, 049903(E) (2004), they pointed out a difficulty of the lattice Boltzmann algorithm in simulations of evaporation.
[45] A. J. Briant, A. J. Wagner, and J. M. Yeomans, Phys. Rev. E **69**, 031602 (2004).
[46] T. Inamuro, T. Ogata, S. Tajima, and N. Konishi, J. Comput. Phys. **198**, 628 (2004).
[47] C. M. Pooley, O. Kuksenok, and A. C. Balazs, Phys. Rev. E **71**, 030501(R) (2005).
[48] A. Onuki, Phys. Rev. Lett. **94**, 054501 (2005).
[49] A. Onuki, Phys. Rev. E **75**, 036304 (2007); in this paper, the energy equation ((2.13)) was integrated, resulting in a parasitic flow around an interface in Figs. 3 and 6.
[50] N. Takada and A. Tomiyama, Int. J. Mod. Phys. C **18**, 536 (2007).
[51] G. Gonnella, A. Lamura, and A. Piscitelli, J. Phys. A: Math. Theor. **41**, 105001 (2008).
[52] A. Kawasaki, J. Onishi, Y. Chen, and H. Ohashi, Comput. Math. Appl. **55**, 1492 (2008).
[53] G. Fang and C. A. Ward, Phys. Rev. E **59**, 417 (1999).
[54] A. Onuki, *Phase Transition Dynamics* (Cambridge University Press, Cambridge, England, 2002).
[55] L. D. Landau and E. M. Lifshitz, *Fluid Mechanics* (Pergamon, New York, 1959).
[56] If we set $e_T = e + \rho \boldsymbol{v}^2/2$ not including the potential U, the term $-\rho \boldsymbol{v} \cdot \nabla U$ appears in the right-hand side of Eq. (2.13) [49].
[57] J. Koplik, J. R. Banavar, and J. F. Willemsen, Phys. Rev. Lett. **60**, 1282 (1988); P. A. Thompson and M. O. Robbins, *ibid.* **63**, 766 (1989); J. L. Barrat and L. Bocquet, *ibid.* **82**, 4671 (1999).
[58] T. Qian, X.-P. Wang, and P. Sheng, Phys. Rev. E **68**, 016306 (2003); T. Qian, C. Wu, S. L. Lei, X.-P. Wang, and P. Sheng, J. Phys.: Condens. Matter **21**, 464119 (2009).
[59] B. Lafaurie, C. Nardone, R. Scardovelli, S. Zaleski, and G. Zanetti, J. Comput. Phys. **113**, 134 (1994); I. Ginzburg and G. Wittum, *ibid.* **166**, 302 (2001); D. Jamet, D. Torres, and J. U. Brackbill, *ibid.* **182**, 262 (2002); S. Shin, S. I. Abdel-Khalik, V. Daru, and D. Juric, *ibid.* **203**, 493 (2005).
[60] D. Beysens, C. R. Phys. **7**, 1082 (2006).
[61] A. Onuki and R. A. Ferrell, Physica A **164**, 245 (1990); A. Onuki, Phys. Rev. E **76**, 061126 (2007).
[62] Y. Miura, S. Yoshihara, M. Ohnishi, K. Honda, M. Matsumoto, J. Kawai, M. Ishikawa, H. Kobayashi, and A. Onuki, Phys. Rev. E **74**, 010101(R) (2006).